OPEN ACCESS
IOP Publishing | IMMT
International Journal of Extreme Manufacturing
Int. J. Extrem. Manuf. **6** (2024) 035004 (17pp)
https://doi.org/10.1088/2631-7990/ad2e14

Vibration-assisted vat photopolymerization for pixelated-aliasing-free surface fabrication

Han Xu[1,2], Renzhi Hu[3], Shuai Chen[3], Junhong Zhu[3], Chi Zhou[4] and Yong Chen[1,2,3,*]

[1] Center for Advanced Manufacturing, University of Southern California, Los Angeles, CA 90007, United States of America
[2] Daniel J. Epstein Department of Industrial and Systems Engineering, University of Southern California, Los Angeles, CA 90089, United States of America
[3] Department of Aerospace and Mechanical Engineering, University of Southern California, Los Angeles, CA 90089, United States of America
[4] Department of Industrial and Systems Engineering, University of Buffalo, Buffalo, NY 14260, United States of America

E-mail: yongchen@usc.edu

Received 27 October 2023, revised 12 December 2023
Accepted for publication 28 February 2024
Published 22 March 2024

Abstract

Mask image projection-based vat photopolymerization (MIP-VPP) offers advantages like low cost, high resolution, and a wide material range, making it popular in industry and education. Recently, MIP-VPP employing liquid crystal displays (LCDs) has gained traction, increasingly replacing digital micromirror devices, particularly among hobbyists and in educational settings, and is now beginning to be used in industrial environments. However, LCD-based MIP-VPP suffers from pronounced pixelated aliasing arising from LCD's discrete image pixels and its direct-contact configuration in MIP-VPP machines, leading to rough surfaces on the 3D-printed parts. Here, we propose a vibration-assisted MIP-VPP method that utilizes a microscale vibration to uniformize the light intensity distribution of the LCD-based mask image on VPP's building platform. By maintaining the same fabrication speed, our technique generates a smoother, non-pixelated mask image, reducing the roughness on flat surfaces and boundary segments of 3D-printed parts. Through light intensity modeling and simulation, we derived an optimal vibration pattern for LCD mask images, subsequently validated by experiments. We assessed the surface texture, boundary integrity, and dimensional accuracy of components produced using the vibration-assisted approach. The notably smoother surfaces and improved boundary roughness enhance the printing quality of MIP-VPP, enabling its promising applications in sectors like the production of 3D-printed optical devices and others.

* Author to whom any correspondence should be addressed.

2631-7990/24/035004+17$33.00

Supplementary material for this article is available online

Keywords: additive manufacturing, vat photopolymerization, piezo vibration, sub-pixel resolution, aliasing

1. Introduction

Additive manufacturing (AM) offers a revolutionary fabrication approach for rapidly converting computer-aided design (CAD) models into solid parts [1], allowing for swift *in-situ* prototyping and mass product customization [2]. Among the many AM processes, mask image projection-based vat photopolymerization (MIP-VPP) is increasingly used in industries such as dental, biomedical, and consumer devices, to name a few, due to its ability for high-speed [3, 4], large-scale [5–7], and high-resolution [8–11] fabrication using digitally patterned ultra-violet (UV) radiation to initiate localized photopolymerization and transform liquid resin into solid products. The versatility of this approach significantly extends the application range of MIP-VPP, moving beyond structural prototyping to various functional product manufacturing, such as microfluidic devices, micro-robotics, optics, and sensors, among others [8, 9, 12–17].

A notable difficulty of MIP-VPP processes is the presence of rough surfaces [18], primarily originating from two aspects: layer stepping and pixelated aliasing [19]. Layer stepping arises when a set of 2.5-dimensional layers is employed to approximate a three-dimensional (3D) model, resulting in a 'staircase' effect on the surface in the *Z*-direction [20]. On the other hand, pixelated aliasing originates from the mask image device, where pixel dimensions and shapes inherently limit the contour's smoothness [21]. Especially for the liquid crystal display (LCD)-based MIP-VPP process, the mask images consist of an array of LCD elements with characteristic sizes between 10 μm–100 μm, with 50 μm elements typically used [22]. The sliced layers from CAD models are represented by a mask image defined by the LCD elements, whose resolution is limited to its pixel size, as shown in figures 1(a)–(c). Consequently, the pixelation of mask images causes an aliasing effect, leading to rough contours on the printed parts, as shown in figures 1(d) and (e). Furthermore, LCD mask images have 'dark zones'—areas where the light intensity between two adjacent pixels is less intense than at the pixel centers, as shown in figure 1(c). The diminished light intensity within these 'dark zones' is inadequate for curing the liquid resin, resulting in rough surfaces on the *XY* plane, as illustrated in figure 1(f).

Extensive research has been conducted to reduce layer stepping and pixelated aliasing in MIP-VPP printed products, mainly for a digital light processing (DLP) system consisting of a digital micromirror device (DMD) and an optical system. The common strategy to address layer stepping is to reduce layer thickness during printing. Techniques that have been developed include continuous liquid interface production, a zooming-focused MIP-VPP, and adaptive slicing MIP-VPP [3, 8, 23]. All of these operate based on this principle. Several post-processing methods have also been proposed and implemented, such as applying various coatings or post-machining processes to smooth out the layer-induced roughness [24–26]. Limited methods exist to reduce pixelated aliasing in the LCD-based MIP-VPP. Traditional techniques, such as gray-scale mask images and pixel blending [26–28], have been developed to diminish pixelated aliasing in the DMD-based MIP-VPP. However, these cannot be used in LCD-based MIP-VPP because the LCD is in direct contact with the building platform through a thin fluorinated ethylene propylene film. Hence, no optical system can be added between them to adjust the focus of the LCD mask image. Most commercial LCD-based 3D printers, such as AnyCubic™, Elegoo™, and Creality™, use this direct contact configuration. The lack of pixel blending between neighboring pixels in such LCD-based MIP-VPP systems presents a significant challenge, motivating us to develop a new approach to address their inherited pixelated aliasing defects. There have been only a few attempts to reduce 'dark zone' aliasing in the LCD-based MIP-VPP systems. For instance, a defocusing MIP-VPP has been proposed to reduce 'dark zone' aliasing by increasing the gap between the LCD and the printing surface [19]. However, this solution potentially compromises dimensional accuracy and resolution. Another approach uses oscillation-assisted DLP to equalize the DMD's light intensity for optical printing [15]. The approach is inspiring, but its use for engineering applications beyond optical lenses is unclear. A general method that can comprehensively reduce boundary segments and 'dark zone' aliasing without compromising dimensional accuracy and resolution is desired for the LCD-based MIP-VPP process.

Here, we report a vibration-assisted MIP-VPP process for the LCD-based configuration to reduce pixelated aliasing effects while maintaining good dimensional accuracy. In vibration-assisted MIP-VPP, the exposure of a stationary mask image is replaced by one that is vibrated in the *X* and *Y* directions. A low-frequency vibration (2–3 Hz) with sub-pixel amplitudes (10–50 μm) is added to the LCD mask images to achieve uniform light intensity. The vibration pattern and amplitude of the LCD panel are designed by a computationally modeled light intensity distribution of mask images. The 3D-printed test cases show a 6-fold improvement in boundary segment roughness (from 6.5 μm to 1.1 μm) and a 3.5-fold improvement in surface roughness (from 0.237 μm to 0.067 μm). The dimensional error of the vibration-assisted MIP-VPP is controlled within a single pixel's size. Finally, we demonstrate test cases with an excellent optical resolving capability suitable for potential 3D-printed optics.

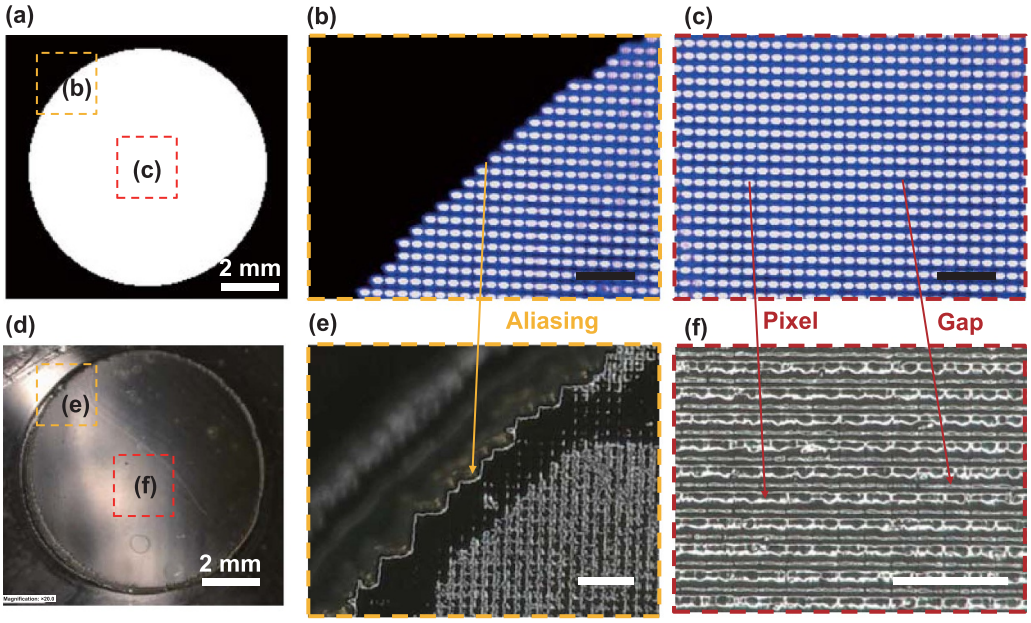

Figure 1. Rough surface of the parts printed by LCD-based MIP-VPP due to the pixelated aliasing. (a) The mask image used to print a cylinder test case, scale bar: 2 mm; (b) the contour aliasing on the edge of the mask images, scale bar: 250 μm; (c) the 'dark zone' aliasing in the gap between two pixels, scale bar: 250 μm; (d) the printed cylinder test case, scale bar: 2 mm; (e) the rough contour of the printed cylinder test case due to contour aliasing, scale bar: 250 μm; and (f) rough surface of the printed cylinder test case due to the 'dark zone' aliasing, scale bar: 250 μm.

2. Experimental section

This section describes the materials, equipment, and methods employed in our study to implement, investigate, and evaluate the vibration-assisted MIP-VPP process.

2.1. Vat photopolymerization material

A commercial photocurable polymer, AnyCubic Clear resin (AnyCubic™, Shenzhen, China), was used in the experiments. The resin was chosen due to its transparency, so we can easily observe the surface roughness. The curing time of the selected resin is ∼6 s for the tested printer, and the curing wavelength is 405 nm.

2.2. Piezo vibration actuator

An in-house developed vibration-assisted MIP-VPP apparatus was used in this study. The parameters of the main components used in the apparatus are listed as follows.

Piezo actuator: the piezo actuators used for the *XY* vibration of the LCD screen are two Piezo actuators (PC4QQ, 18.0 μm Max Displacement, size 6.5 mm × 6.5 mm × 18.0 mm). The resonant frequency is 65 kHz, and the maximum load at maximum displacement is 400 N. The recommended drive voltage limit is 150 V. The piezo actuators were driven by two voltage drivers (Piezo Master, MODEL VP7206) controlled by a microcontroller (Arduino Due). The schema plot and the practical photo of the piezo actuator and its controller are shown in figure S1.

Vibration amplifier: to enlarge the maximum displacement of the piezo actuator, a pair of two-stage mechanical amplification structures was utilized as vibration amplifiers. These amplifiers can achieve 5× magnification of the displacement of the piezo actuator, ensuring adequate range and precision for the mask image vibration. The CAD design and the practical assembly of the piezo amplifier are illustrated in figure S2. The CAD design demonstrates that the deformation of the piezo actuators acts on a flexible-hinged, diamond-shaped mechanical amplifier, which in turn pushes the center plate in the target direction. The physical assembly shows two amplifiers stacked together and connected by the center plate to facilitate shifting movement in both *X* and *Y* directions. The bottom amplifier is fixed on the optical table, while the top amplifier is attached to the LCD mount.

The resolution of the piezo actuator after amplification was investigated. The displacement corresponding to voltage was measured using a series of images of the piezo stage taken under 386× magnification by a SOL 161 optical microscope (MicroVu, Windsor, CA). The image resolution was 680 × 480. The analog output of the DAC pin ranged from 0.53 V to 2.75 V, translating to input voltages of the piezo actuator from 31.53 V to 165 V. Initially, input voltages ranging from 31.53 V to 138.30 V were applied sequentially to expand the piezo actuator. Subsequently, input voltages from 138.30 V to 31.53 V were used to shrink the piezo actuator. The platform's position corresponding to each input voltage

Table 1. Slicing and printing parameters.

CAD model	Layer thickness (μm)	Pixel size (μm)	Exposure time (s)	Layer numbers
9 mm cylinder	50	50	5	60
Isosceles right triangle	50	50	5	60
Transparent disc	50	50	5	40

was captured by the optical microscope under 386× magnification and measured through image processing. The displacement of the piezo actuator in the *XY* direction is presented in tables S1 and S2. By controlling the input voltage, a 5 μm resolution of the displacement of the piezo linear stage was achieved, demonstrating the accuracy of the mask image vibration control.

LCD: the LCD screen used for the photomask is an Elegoo™ Mars 2pro 5.5 inches LCD monochrome screen (Sharp04 SX04 2K LCD). The resolution of the LCD is 1440 × 2560 with a pixel size of 50 μm. The LCD screen is mounted on piezo actuators, which can shift the screen in both *X* and *Y* directions based on input voltages. The controlled mask image-shifting process is illustrated in figure S3. Figure S3(a) presents a schematic diagram of the piezo actuator control mechanism using voltage signals. Two square waves were employed to manage mask image shifting in the *X* and *Y* directions independently. Figures S3(b) and (c) demonstrate the actual mask image-shifting in the *X* and *Y* directions, respectively, as the voltage varies from 31.5 V to 138.3 V. The camera remains stationary during the mask image-shifting process. The measured distance of relative mask image shifting matches the travel distance of the piezo actuator.

Other hardware: the experimental hardware setup is depicted in figure S4. It consists of a vertically-oriented linear stage (Motorized XSlide™ XN150 Series—Lead Screw) with a straight-line accuracy of 0.003”/10” (0.076 mm per 250 mm) and repeatability of 0.000 1 inch (0.002 54 mm). An Elegoo Mars Pro 2 resin tank was mounted on a fixed optical table. An Arduino Due microcontroller was employed to coordinate the motion of the linear stage, the projection of mask images, and the vibration of the piezo stages. A 405 nm UV light-emitting diode (LED) module (UV_A MODULE 6565S) with collimator lenses was used to generate a uniform UV light source for the LCD screen. Besides, a touchscreen control panel was incorporated into the setup for commanding the experimental process. Additionally, a 350 W and 12 V power supply was used to provide power to the whole system.

2.3. Test case design and printing

Surface roughness test case: a cylinder test case whose diameter is 9 mm and height is 3 mm was printed to study the effect of the vibration on surface roughness. The CAD model of the test case was drawn using SolidWorks™. A commercial slicing software, Chitubox, was used to generate the mask images and the G-codes for the LCD-based 3D printer. The parameter settings of the slicing and printing are shown in table 1. After printing, the 3D-printed samples were cleared in 99.5% IPA for 5 min, followed by pressured airflow cleaning for 10 s.

Table 2. Parameter setting of the CCD camera.

CCD camera parameters	Set value
Brightness	0
Contrast	32
Hue	0
Saturation	64
Sharpness	3
White balance	4 600
Backlight compensation	1
Exposure	−7

Boundary segments aliasing test case: an isosceles right triangle test case whose length is 1 mm was printed to study the effect of vibration on boundary segments aliasing. The same CAD and slicing software and cleaning process were used. The grayscale mask image was generated by Chitubox with its anti-aliasing setting. The grayscale values of the pixels were calculated based on geometric heuristics [27].

Dimensional accuracy test case: both the isosceles right triangle and circle test cases with reduced lengths or diameters (at 2 000 μm, 1 000 μm, 500 μm, and 200 μm) were printed. The same CAD and slicing software and cleaning process were used.

Resolving capability test case: a test case of a circular disc whose diameter is 9 mm and thickness is 2 mm was printed. The same CAD and slicing software and cleaning process were used.

2.4. Light intensity measurement

The light intensity of the LCD pixels was measured by a charge-couple device (CCD) camera (pluggable USB Digital Microscope, Pluggable technology, US). The camera resolution is 1600 × 900. The CCD camera was controlled by a Digital Viewer, the settings of which are shown in table 2. The captured images were converted to grayscale images by ImageJ to measure the brightness of each pixel.

2.5. Surface roughness characterization

The surface roughness of printed samples was evaluated by a profilometer, SURFTEST SJ-410 (Mituyo Corporation, Japan). The sample length was 0.5 mm. The boundary segment

aliasing was calculated based on microscope images captured by a Keyence microscope. The resolution of the image was 0.77 μm pixel^{-1}.

2.6. Resolving capability characterization

The resolving capability of printed samples was evaluated using optical microscopy images captured by the Micro-Vu Sol system at a magnification rate of 64×. The resolving capability was characterized by calculating the modulation transfer function (MTF) from the images of a USAF 1951 resolution target.

3. Results

3.1. Light intensity distribution of LCD mask image

The 'dark zone' on the LCD mask images accounts for the rough surface in the *XY* plane. We first analyzed the light intensity of the LCD mask image on the VPP's building platform. We quantified the 'dark zone' on the mask image by examining the light intensity variation. We studied the relationship between the 'dark zone' and the light intensity distribution of a single LCD pixel. A CCD camera measures the relative light intensity maps of the whole LCD mask image. The resulting two-dimensional brightness maps are normalized to represent the relative light intensity in the *XY* plane, where 100% represents the maximum (255) brightness of the captured image.

Light intensity significantly drops between two adjacent pixels in both *X* and *Y* directions and by various amounts. Figure 2(a) shows that the light intensity in the *X* direction exhibits a maximum 17% intensity drop at the 'dark zone'. Figure 2(b) presents that the convoluted light intensity in the *Y* direction exhibits a maximum 55% intensity drop at the 'dark zone'. The LCD screen used in MIP-VPP causes this light intensity variation (figure S9). Besides, the span of the 'dark zone' region in the *X* direction, which is characterized by the region with light intensity lower than 95% of the maximum, is 13 μm. In comparison, the span of the 'dark zone' region in the *Y* direction is 24 μm. Since the photopolymerization result is determined by the accumulated UV dosage, governed by the Jacobi equation: $C_\mathrm{d} = \delta \ln\left(\frac{T_\mathrm{d}}{T_\mathrm{c}}\right)$ [29], the decrease of light intensity in the 'dark zone' leads to insufficient curing between adjacent pixels. The 'dark zone' in the light intensity map is consistent with the surface texture observed in the printed sample in figure 1(f), confirming the influence of light intensity variation on surface roughness.

To study the cause of the 'dark zone', we measured the relative light intensity of individual pixels on the LCD mask image using the same method. As shown in figure 2(c), the relative light intensity of a single pixel has an ellipse footprint, revealing an anisotropic light intensity distribution in the *X* and *Y* directions. Figure 2(d) illustrates the light intensity distribution in the *X* direction. Here, we regard the variation of light intensity smaller than 95% of the maximum as the stable light intensity, primarily attributed to the curing of the resin. The region of stable light intensity spans $x_\mathrm{P} = 35\,\mu$m in the *X* direction, and the light intensity quickly drops below the curing threshold outside the stable region. Figure 2(e) presents the light intensity distribution in the *Y* direction, where the region of stable light intensity measures $y_\mathrm{P} = 25\,\mu$m. Figure 2(f) shows the 3D light intensity distribution of a single pixel, which is close to an elliptical super-Gaussian distribution. Since LCD pixels are assembled in $\delta_\mathrm{p} = 50\,\mu$m interval, the span of 'dark zone' region for a single pixel is $\delta_\mathrm{p} - x_\mathrm{P} = 15\,\mu$m in the *X* direction, and $\delta_\mathrm{p} - y_\mathrm{P} = 25\,\mu$m in the *Y* direction. This result is close to the span of the 'dark zone' in the whole mask image. A slightly larger span of the 'dark zone' in the single pixel light intensity distribution is because it lacks supporting light from adjacent pixels.

An elliptical super-Gaussian model is used to describe the light intensity distribution of each pixel. Relative light intensity sampled from figure 2(c) is used to fit the super-Gaussian model:

$$I = \exp\left(-\left(\frac{(x-x_0)^2}{2{\sigma_x}^2} + \frac{(y-y_0)^2}{2{\sigma_y}^2}\right)^p\right). \tag{1}$$

The sample points of the measured light intensity are shown in table S3. The fitted elliptical super-Gaussian model is shown in table S4. Both the standard deviation and the *p*-value verify the fidelity of the super-Gaussian model. We compared the super-Gaussian model with the practical light intensity distribution in figure S11, demonstrating the simulation model's good fidelity. Figure 2(g) visualizes the elliptical super-Gaussian model of the light intensity distribution. Accordingly, the convoluted light intensity distribution of an LCD mask image can be simulated from the super-Gaussian model. For example, the convoluted light intensity distribution of a 5 × 5 pixels array is simulated and shown in figure 2(h). It can be found that the span of the light intensity model is smaller than the period of LCD pixels, leading to 'dark zone' regions in the *XY* plane.

An essential issue in an LCD-based MIP-VPP system is the relative light intensity of the LCD mask images is a convoluted light intensity of all the single pixels; however, the nonuniform light intensity in the LCD's individual pixels contributes to the 'dark zone' aliasing on the photocuring surface. Minimizing the 'dark zone' regions is vital to reduce the printed parts' surface roughness. Instead of increasing the gap between the LCD and printing surface to reduce 'dark zone' aliasing [19], we propose a vibration-assisted MIP-VPP process for the LCD-based systems.

3.2. Schema of vibration-assisted MIP-VPP

Guided by the LCD light intensity simulation, a vibration-assisted MIP-VPP system is presented to generate a more uniform light intensity of an LCD mask image and eliminate pixelated aliasing. From the previous work for the DMD-based MIP-VPP systems [28, 30], we observed that a mask image's shape and light intensity can be tuned by dividing the one-shot UV exposure into multiple exposures, each with a slight shift in the *XY* directions. Inspired by this, we deduced the

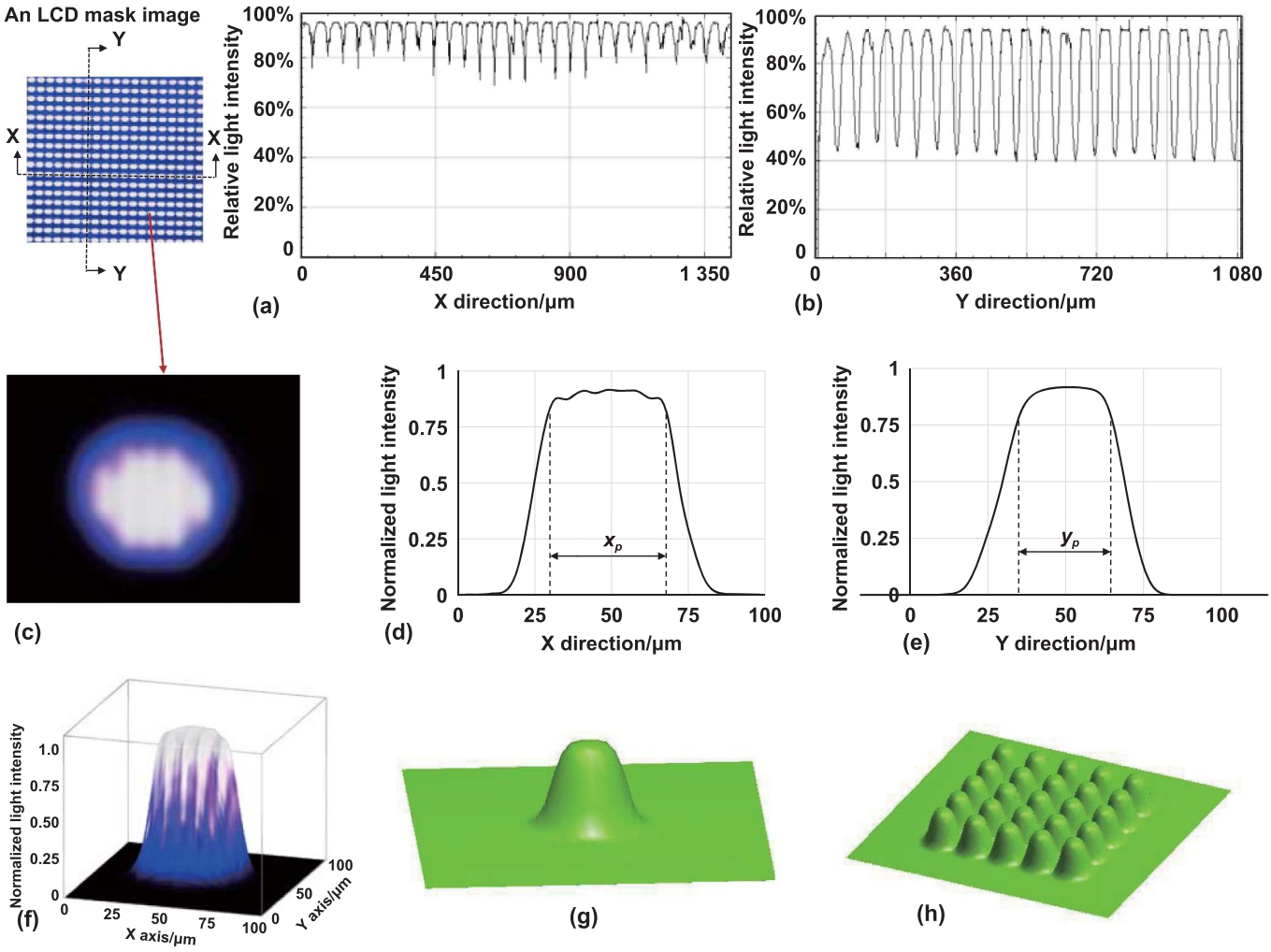

Figure 2. The relative light intensity of an LCD mask image. (a) The relative light intensity map of the LCD mask image in the *X* direction; (b) the relative light intensity map of the LCD mask image in the *Y* direction; (c) the top view of the relative light intensity distribution of a single pixel; (d) the relative light intensity distribution of a single pixel in the *X* direction; (e) the relative light intensity distribution of a single pixel in the *Y* direction; (f) the 3D view of the relative light intensity distribution of a single pixel; (g) the simulation of a single-pixel light intensity by the elliptical super-Gaussian model; and (h) the simulation of the light intensity of a 5 × 5 LCD array by the elliptical super-Gaussian model.

light intensity nonuniformity of LCD pixels can be mitigated by replacing the exposure of a stationary mask image with the exposure of a vibrating mask image, under precisely controlled moving steps and amplitudes over time.

The schema of the vibration-assisted MIP-VPP process is illustrated in figure 3(a). In the vibration-assisted MIP-VPP process, the LCD photomask vibrates between designated positions, which are referred to as *steps*. The mask image on the LCD screen remains unchanged while printing the same layer. The general vibration pattern of the LCD mask images is parameterized, as shown in figure 3(b). The vibration pattern of the mask images is noted as $a \times b$ steps, where a and b are the number of the steps in the X and Y directions, respectively. In total, the mask image will travel through $a \times b$ positions in one-layer printing. The convoluted light intensity without vibration is denoted as a 1-step vibration, and an n-step vibration divides the one-layer exposure into n sub-exposures. Each sub-exposure takes an equal amount of time, and the sum of all the sub-exposure times remains the same as the original exposure time. For example, if the curing time of a resin is 6 s and a 16-step vibration is used, the sub-exposure time at each step is 0.375 s. The moving time of the piezo actuator is negligible due to its fast response time (<1 ms) of the piezo actuator compared to the applied vibration interval (>100 ms) [31, 32]. Consequently, the equivalent light intensity of each sub-exposure is $1/n$ of the entire exposure. The travel distance between two consecutive steps is determined by dividing the pixel size by the number of vibration steps in the X and Y directions. The mask image is shifted sequentially to positions 1, 2, 3, …, and up to $a \times b$. After reaching the $a \times b$ position, the mask image returns to position 1 for the next layer, creating a cyclical vibration pattern. Figure 3(c) presents an example of a potential vibration pattern, where the LCD panel is shifted to six different positions, dividing one LCD pixel into six sections. This parameterization allows for precise control of the vibration pattern, optimizing surface quality by adjusting

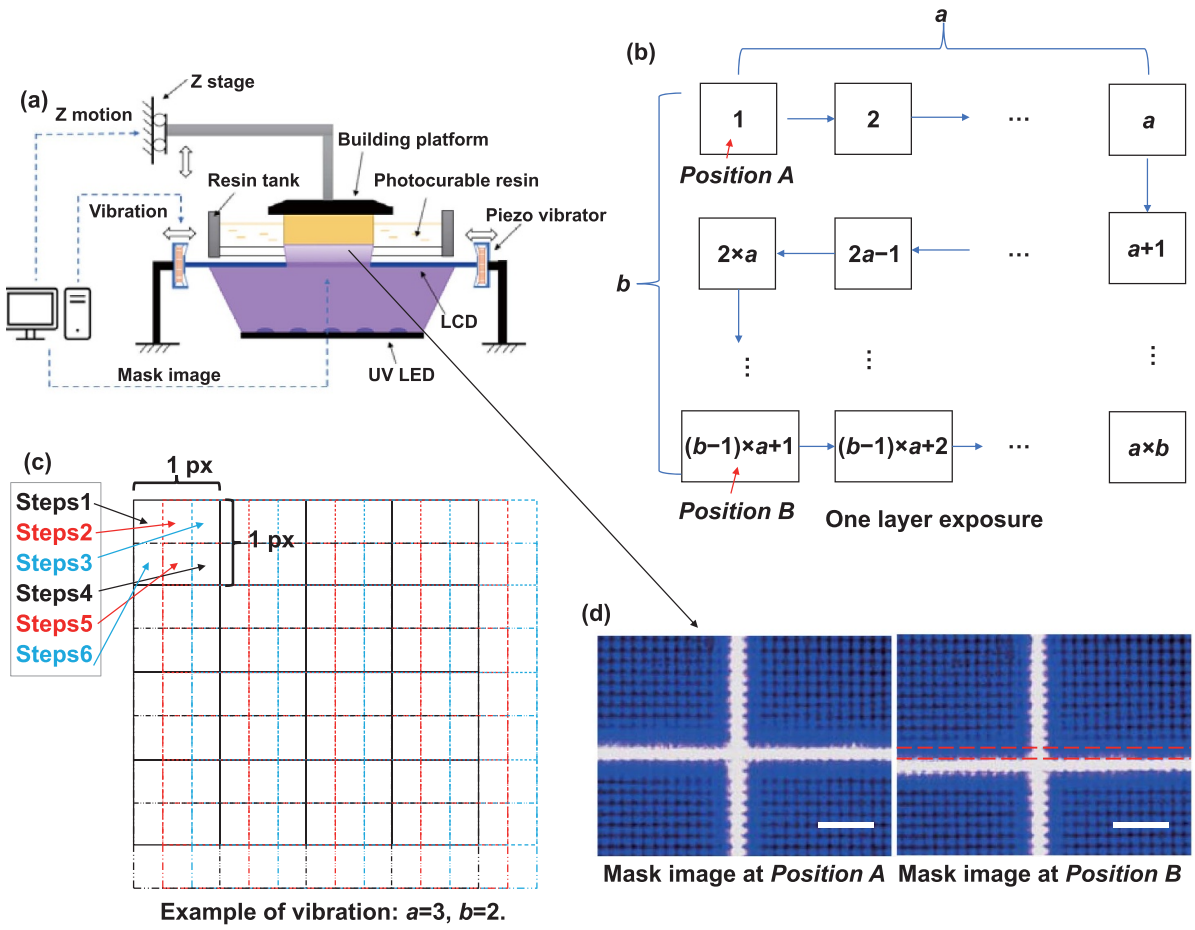

Figure 3. The schema of the vibration-assisted MIP-VPP process using LCD. (a) The hardware configuration of the vibration-assisted MIP-VPP apparatus; (b) the general pattern of $a \times b$ mask image vibration, a and b are the numbers of steps in row and column, respectively; (c) an example of a 2×3 steps mask image vibration; and (d) the microscale shifting of the LCD mask image actuated by a piezo actuator, scale bar: 250 μm.

the number of vibration steps and the travel distance in both X and Y directions

We implemented the vibration-assisted MIP-VPP using an in-house-built XY piezo actuator, a commercial LCD screen, a UV LED light source, and a Z linear stage. The UV light emitted from the LED light source is modulated by the LCD photomask, selectively curing the liquid resin on the building platform. The primary hardware adaptation for the vibration-assisted MIP-VPP system involves mounting the LCD photomask on an XY piezo actuator, which enables a high-resolution (5 μm) vibration of mask images in both X and Y directions. Figure 3(d) shows one-pixel distance (50 μm) mask image shifting enabled by a Y-direction piezo actuator. The resin tank, the building platform, the LED UV light source, and the Z stage are fixed to the optical table and isolated from the vibration. A microcontroller synchronizes the Z stage's motion, the mask images' exposure, and the LCD photomasks' vibration.

We investigated these essential parameters by simulating the convoluted light intensity of the vibration-assisted LCD mask image using the light intensity of a single pixel to optimize the light uniformity. Figure 2(f) reveals an anisotropic light intensity distribution for a single pixel in the LCD photomask. Given the orthogonality of the X and Y vibrations, their effects on light intensity are independent. We separately examined these directions to understand mask image vibration's impact on 'dark zone' aliasing.

Figure 4 illustrates the simulation of the convoluted light intensity in the X direction. Convoluted light intensities of one, two, three, and four steps represent the vibration patterns 1×1, 2×1, 3×1, and 4×1, respectively. The X-axis represents the position and size of the pixels, while the Y-axis indicates the relatively light intensity. The simulation displays the light intensity of five consecutive pixels to represent the light intensity across the entire mask image. The relative light intensity of each single pixel is depicted in red, and the convoluted relatively light intensity is shown by a black line [28, 30]. The solid red line represents the original position of the light intensity in the LCD mask image without vibration, and the dashed line denotes the shifted mask image positions during vibration.

From figure 4(a), the convoluted light intensity of a 1-step vibration (no vibration) exhibits 17% energy variation at the gap between two neighboring pixels. However, the intensity variation for a 2-step vibration is 8% smaller than that of a 1-step vibration, as shown in figure 4(b). This reduction in variation is due to the shift of the mask image to a new position

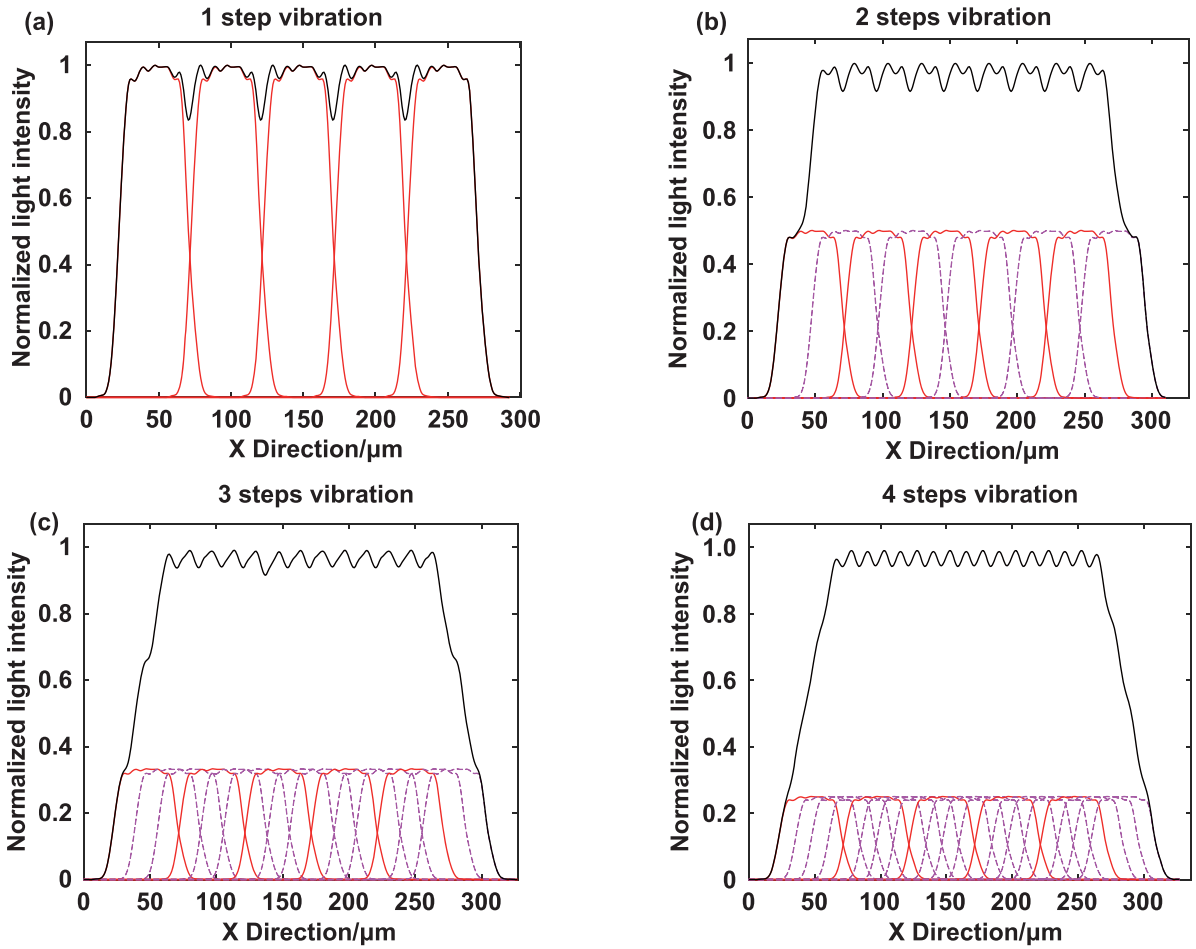

Figure 4. The simulation of the convoluted light intensity in the *X* direction. (a) With a 1-step vibration (i.e. static without any movement); (b) with a 2-step vibration; (c) with a 3-step vibration; and (d) with a 4-step vibration.

between the gaps of the original pixels, which mitigates the nonuniformity caused by the 'dark zone'. Additionally, we note that the convoluted light intensity variation decreases as the number of vibration steps increases. The four-step vibration (figure 4(d)) reduces the light intensity variation by less than 5%, leading to a much smoother surface. The residual light intensity variation observed after applying the vibration steps is due to the light intensity variation of the LCD elements rather than the 'dark zone' aliasing. This indicates that the vibration-assisted approach effectively provides uniform light intensity over the photocuring surface defined by a mask image.

The convoluted light intensity in the *Y* direction is similarly simulated, as shown in figure 5. The simulation of a 1-step vibration reveals a 55% light intensity drop at the gap between pixels. Applying a 2-step vibration to the mask image reduces the valley in the simulated light intensity to less than 10%. An increase of the vibration steps to 3 and 4 results in the light intensity variation being further reduced to less than 7% and 3%, respectively. Notably, the peak light intensity reduces to 80% of its original value after the mask image is vibrated in the *Y* direction in figures 5(c) and (d). This reduction occurs because the light intensity of the initial peak portion is spread out to a broader area. The peak light intensity decreases as the total input energy does not change. The reduced light intensity can be easily compensated by increasing the original exposure time to ensure proper curing while maintaining a smoother surface.

The simulations for both *X* and *Y* directions show a trend where light intensity variation decreases with an increase in the number of vibration steps. Figure 6 illustrates this relationship by calculating light intensity variation based on the differences between the maximum and minimum light intensity values. In the *X* direction (figure 6(a)), light intensity variation starts at 17% for the 1-step vibration, drops to 5% for the 3-step vibration, and decreases to 2% for the 6-step vibration. In the *Y* direction (figure 6(b)), the variation begins at 55%, dramatically falls to 5% with 4 steps, and declines to 1% with 6 steps. The difference in steps required to achieve less than 5% variation in the *X* and *Y* directions can be attributed to the 'dark zone' areas being wider in the *Y* direction than in the *X* direction. As a result, the *Y* direction needs more shifting steps to fill the 'dark zone' gap. Considering LCD elements' intrinsic light intensity variation, we used a 5% variation threshold to select the desired vibration pattern. Following this model, a 3-step vibration in the *X* direction and a 4-step vibration in the *Y* direction could be selected for all the MIP-VPP printers using the studied LCD screen, i.e. a vibration of 3 × 4 steps

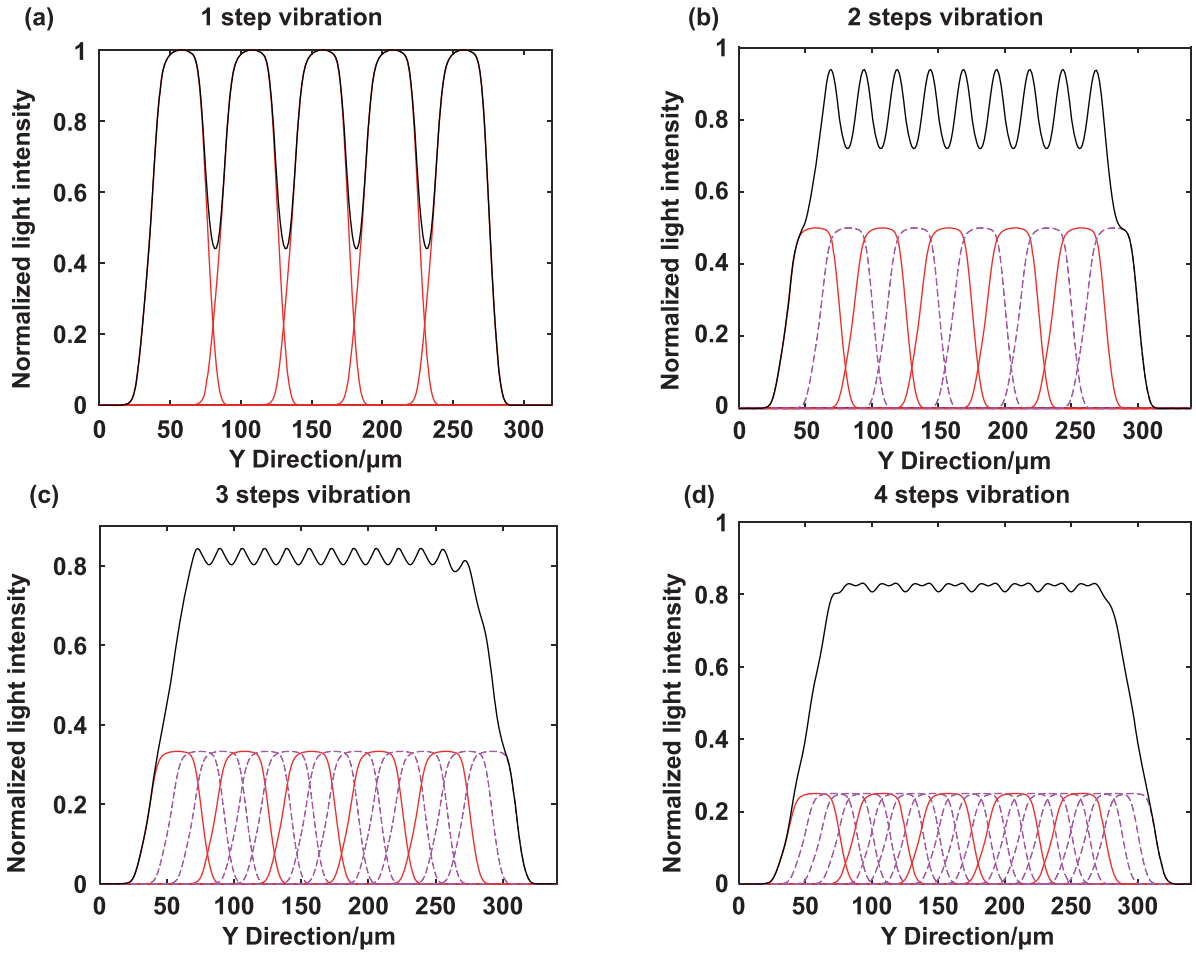

Figure 5. The simulation of the convoluted light intensity in the *Y* direction: (a) with a 1-step vibration (i.e. static without any movement); (b) with a 2-steps vibration; (c) with a 3-steps vibration; (d) with a 4-steps vibration.

can be applied. The simulation of the convoluted light intensity distribution in the *XY* plane over different vibration steps is demonstrated in figure S6. The light intensity variation in the *XY* plane is negligible after applying vibration with 3 × 4 or even more steps.

3.3. Experimental results of the vibration-assisted MIP-VPP process

In this section, we present the experimental results of the vibration-assisted MIP-VPP, and discuss the impact of the mask image vibration on surface roughness, boundary segment aliasing, dimensional accuracy, and optical resolving capability of the 3D-printed parts.

To verify the impact of the vibration-assisted MIP-VPP process on surface roughness, we printed a cylinder with a 9 mm diameter and evaluated its top surface's roughness. The vibration patterns of 1 × 1 (no vibration), 2 × 2, and 3 × 4 were printed under identical layer exposure time and thickness. The top surface of the printed samples was observed using an optical microscope, and the surface profile of the samples was measured using a profilometer, as shown in figure 7. The grid textures in figures 7(b) and (d) are discernible in the images of the samples printed without vibration and with a 2 × 2 steps vibration. Further, these grid textures on the 3D-printed surface are identical to the convoluted light intensity distribution patterns shown in figures 7(a) and (d). Such shape correspondence verifies the light intensity distribution of an LCD mask image determines the surface texture of the LCD-based MIP-VPP process. As the vibration steps increase, the grid texture in figure 7(h) becomes less prominent, suggesting that surface roughness decreases with an increasing number of vibration steps. The decrease in surface roughness can also be explained by the uniform light intensity distribution after 3 × 4 steps vibration, as shown in figure 7(g).

Figures 7(c), (f) and (i) on the right show the surface profile in the *X* direction, and the measured length is 500 μm. From the surface profile of the non-vibration printed test case, we can observe the periodic bumps have an amplitude of 0.7 μm. The period of the bumps is ∼50 μm, which is consistent with the pixel size. This also confirms that pixelated aliasing is the main reason for the rough surface occurring in the LCD-based MIP-VPP. When the 2 × 2 steps vibration is applied to the LCD mask image, the amplitude of the bumps decreases to 0.3 μm. This result suggests that the 2 × 2 steps vibration

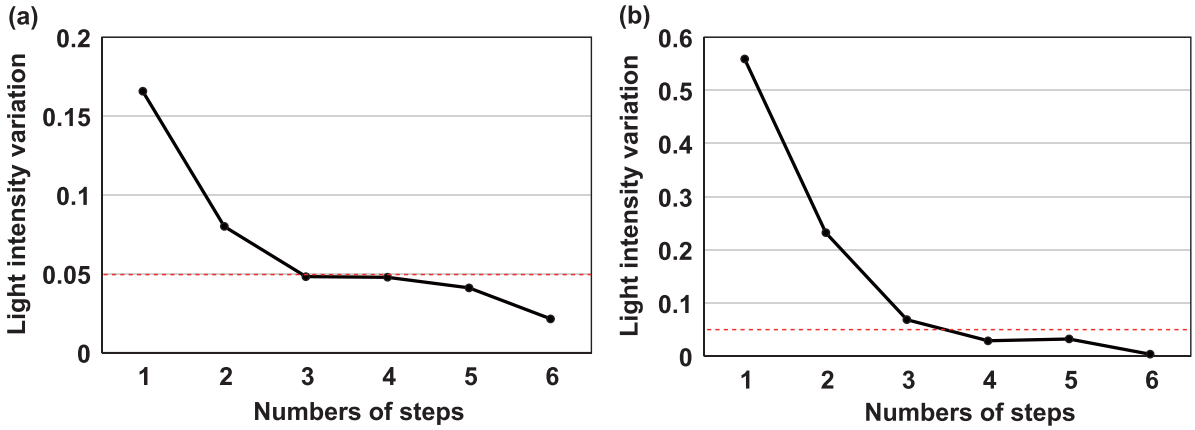

Figure 6. The relationship between the light intensity variation and the number of vibration steps. (a) The light intensity variation in the *X* direction; and (b) the light intensity variation in the *Y* direction.

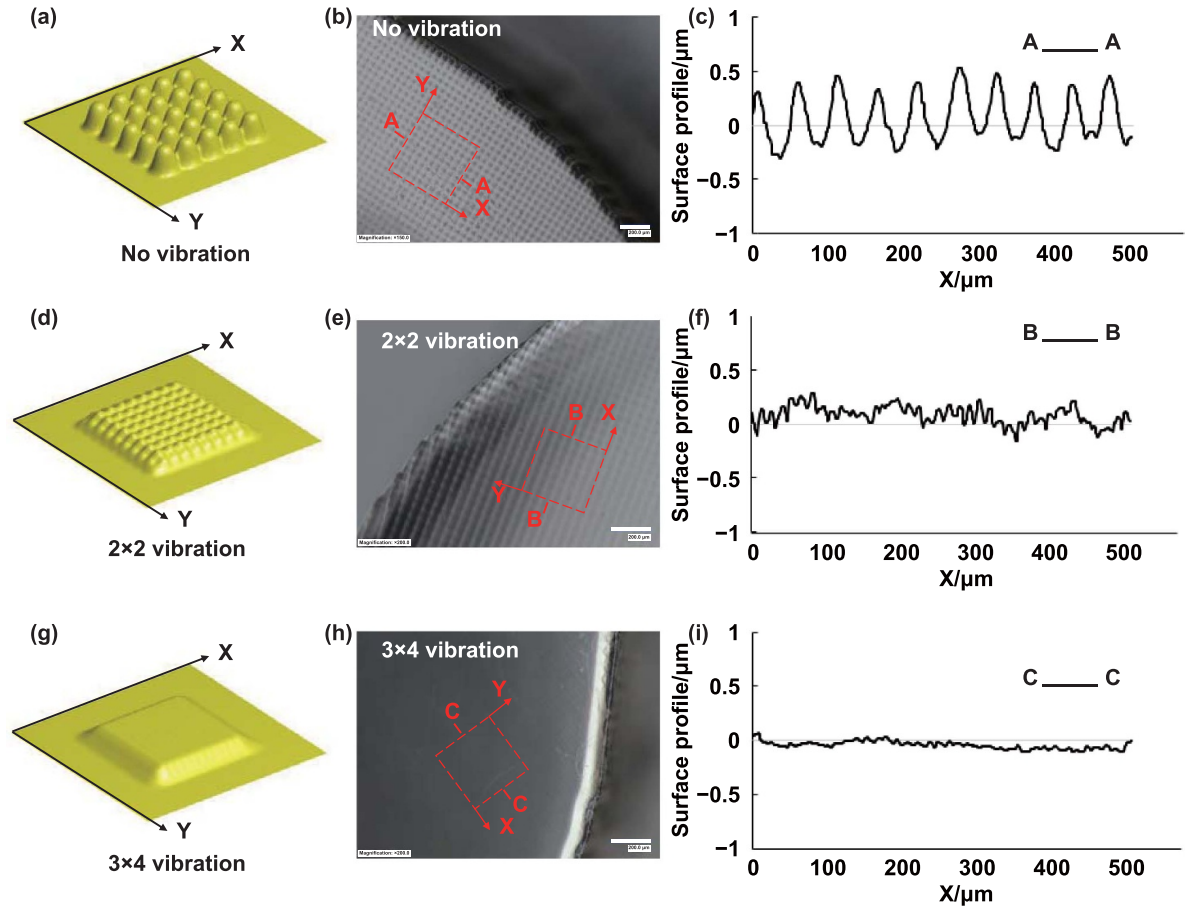

Figure 7. Textures on the top surface of the 3D-printed disc test cases under different vibration steps, scale bar: 200 μm. (a) The light intensity distribution of the mask image without vibration; (b) the texture on the top surface and (c) its surface profile of the disc test case printed by MIP-VPP without vibration; (d) the light intensity distribution of the mask image with a 2 $\times$ 2 steps vibration; (e) the texture on the top surface and (f) its surface profile of the disc test case printed by MIP-VPP with a 2 $\times$ 2 steps vibration; (g) the light intensity distribution of the mask image with a 3 $\times$ 4 steps vibration; (h) the texture on the top surface and (i) its surface profile of the disc test case printed by MIP-VPP with a 3 $\times$ 4 steps vibration.

reduced light intensity variation between its peak and valley by over half. The period of the bumps at the 2 $\times$ 2 steps vibration is reduced to the average of 25 μm, which is consistent with the light intensity simulation in 2 $\times$ 2 steps vibration. When 3 $\times$ 4 steps vibration was applied to the printing, the surface profile showed a maximum amplitude smaller than 1 μm, significantly smaller than the 2 $\times$ 2 steps vibration surface. The surface roughness R_{ms} in the *X* direction of no

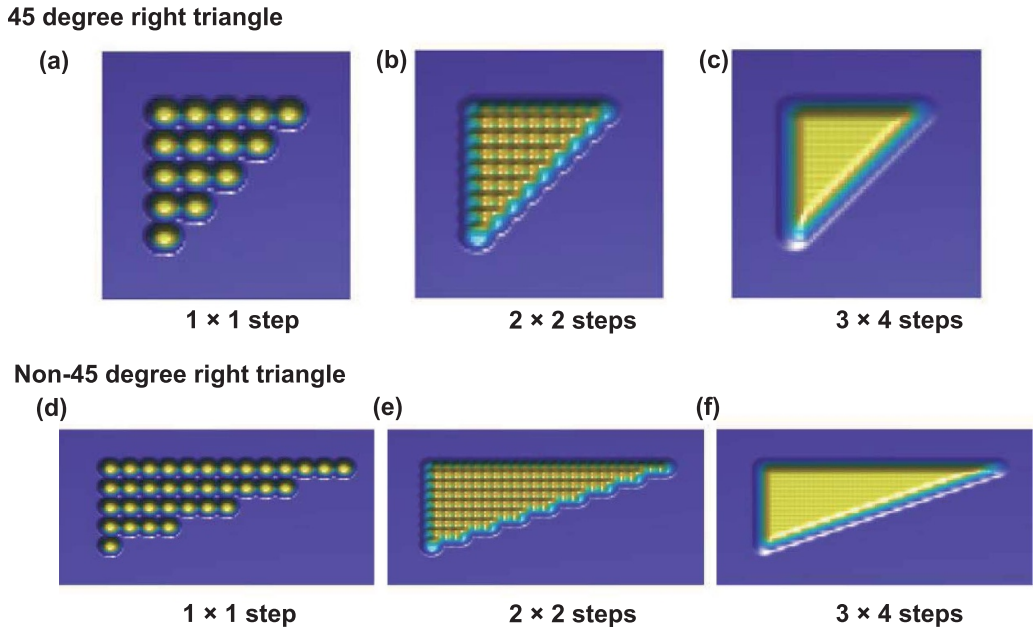

Figure 8. The simulated results of the boundary segment roughness based on the convoluted light intensity distribution of vibration-assisted MIP-VPP. (a) The simulated curing result of a 45-degree right-triangle test case without vibration; (b) the simulated curing result of the 45-degree right-triangle test case with a 2 × 2 steps vibration; (c) the simulated curing result of the 45-degree right-triangle test case with a 3 × 4 steps vibration; (d) the simulated curing result of non-45-degree right-triangle test case without vibration; (e) the simulated curing result of non-45-degree right-triangle test case with a 2 × 2 steps vibration; and (f) the simulated curing result of non-45-degree right-triangle test case with a 3 × 4 steps vibration.

vibration, 2 × 2 steps vibration, and 3 × 4 steps vibration are 0.237 μm, 0.138 μm, and 0.067 μm, respectively. A higher than 3-fold surface roughness improvement is observed using the developed vibration-assisted MIP-VPP.

Besides the 'dark zone' aliasing, the boundary segment aliasing of 3D-printed parts has been studied, as it impacts the boundary segment roughness of the MIP-VPP-printed parts. Figure 8 shows the simulation of the curing results for a set of right-triangle test cases. As seen in figures 8(a)–(c), vibration helps reduce the boundary segments' roughness for both orthogonal and sloped lines. This improvement arises because the vibration-assisted MIP-VPP shifts the mask image within one-pixel amplitude, smoothing out rough features within a pixel size. Vibration can also reduce their roughness for the non-45-degree test cases, as shown in figures 8(d)–(f). However, the results show a saw-tooth-like feature, even with 3 × 4 steps vibration, which can be attributed to the fact that the rough features on the sloped lines span three-pixel sizes in the X direction. Hence, they cannot be entirely smoothed out by a single pixel vibration.

A set of right-angle triangle test cases were printed using the vibration-assisted MIP-VPP system to quantify the boundary segment aliasing improvement. Figure 9 shows a comparison of the boundary segment aliasing of the bottom side and the slant side of the right-angle case. Four scenarios were compared, including binary MIP-VPP (i.e. pixels in mask images are either black or white), grayscale MIP-VPP (i.e. pixels in mask images can be set to transitional values between black and white), vibration-assisted MIP-VPP with binary images, and vibration-assisted MIP-VPP with grayscale images. Figures 9(a) and (b) show the test case profile printed by binary MIP-VPP. The pixelated aliasing can be observed on both slant (30 μm) and bottom (10 μm) sides of the test case. The grayscale MIP-VPP method slightly improves the boundary segment smoothness, as shown in figures 9(d) and (e). However, the pixelated aliasing is still visible. Moreover, applying the grayscale to the mask image makes the 'dark zone' aliasing more severe on the top surface, as shown in figure 9(f). In comparison, vibration-assisted MIP-VPP reduces the boundary segments aliasing to 5 μm on the slant side and 3 μm on the bottom side. The vibration-assisted MIP-VPP using grayscale images achieves slightly smaller boundary segment aliasing than the vibration-assisted MIP-VPP using binary images (figures 9(j) and (k)).

The boundary segment roughness is quantified by the root mean square R_{ms}, which is measured from the bottom side and the slant side profiles of the right-triangle test cases. Table 3 shows the boundary segment roughness of four printing processes for the designed test cases. The boundary segment roughness of the bottom side drops to 29% of the binary MIP-VPP and 63% of the grayscale MIP-VPP. Additionally, the boundary segment roughness of the slant side drops to 25% of the binary MIP-VPP and 40% of the grayscale MIP-VPP. This indicates a significant improvement in boundary segment smoothness when using the developed vibration-assisted technique for MIP-VPP. When comparing the boundary segment smoothness of slant lines and bottom lines, both grayscale and vibration processes have an effect in smoothing the pixelated error and the slope surface. But vibration-assisted MIP-VPP has a more significant impact on smoothing the slope surface,

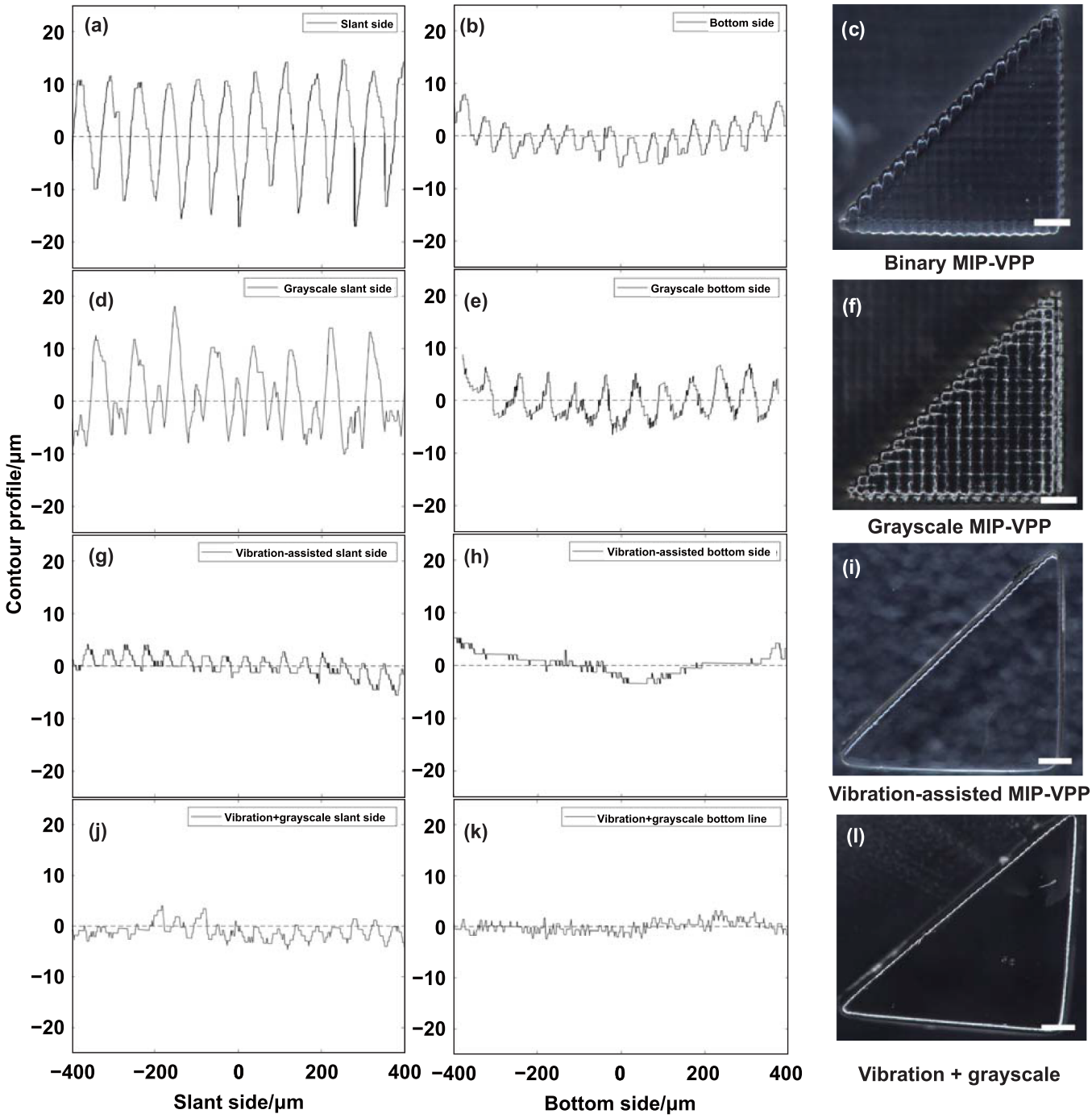

Figure 9. The boundary segments aliasing of the triangle test case, scale bar: 150 μm. (a) The boundary segments profile of the slant side printed by binary MIP-VPP; (b) the boundary segments profile of the bottom side printed by binary MIP-VPP; (c) the triangle test case printed by binary MIP-VPP; (d) the boundary segments profile of the slant side printed by grayscale MIP-VPP; (e) the boundary segments profile of the bottom side printed by grayscale MIP-VPP; (f) the triangle test case printed by grayscale MIP-VPP; (g) the boundary segments profile of the slant side printed by vibration-assisted MIP-VPP; (h) the boundary segments profile of the bottom side printed by vibration-assisted MIP-VPP; (i) the triangle test case printed by vibration-assisted MIP-VPP; (j) the boundary segments profile of the slant side printed by vibration-assisted MIP-VPP combined with grayscale mask image; (k) the boundary segments profile of the bottom side printed by vibration-assisted MIP-VPP combined with grayscale mask image; and (l) the triangle test case printed by vibration-assisted MIP-VPP combined with grayscale mask image.

given by the standard deviation. Moreover, combining grayscale images and the LCD vibration yields the lowest standard deviation values and the smoothest boundary segments. The test cases of other more general polygons, such as non-45-degree triangles and pentagons, are used to quantify the effect of vibration-assisted MIP-VPP on reducing boundary segment

Table 3. The boundary segment roughness R_{ms}.

	Slant side (μm)	Bottom side (μm)
Binary	8.0	6.5
Grayscale	3.0	6.2
Vibration-assisted + binary	2.0	1.9
Vibration-assisted + grayscale	1.8	1.1

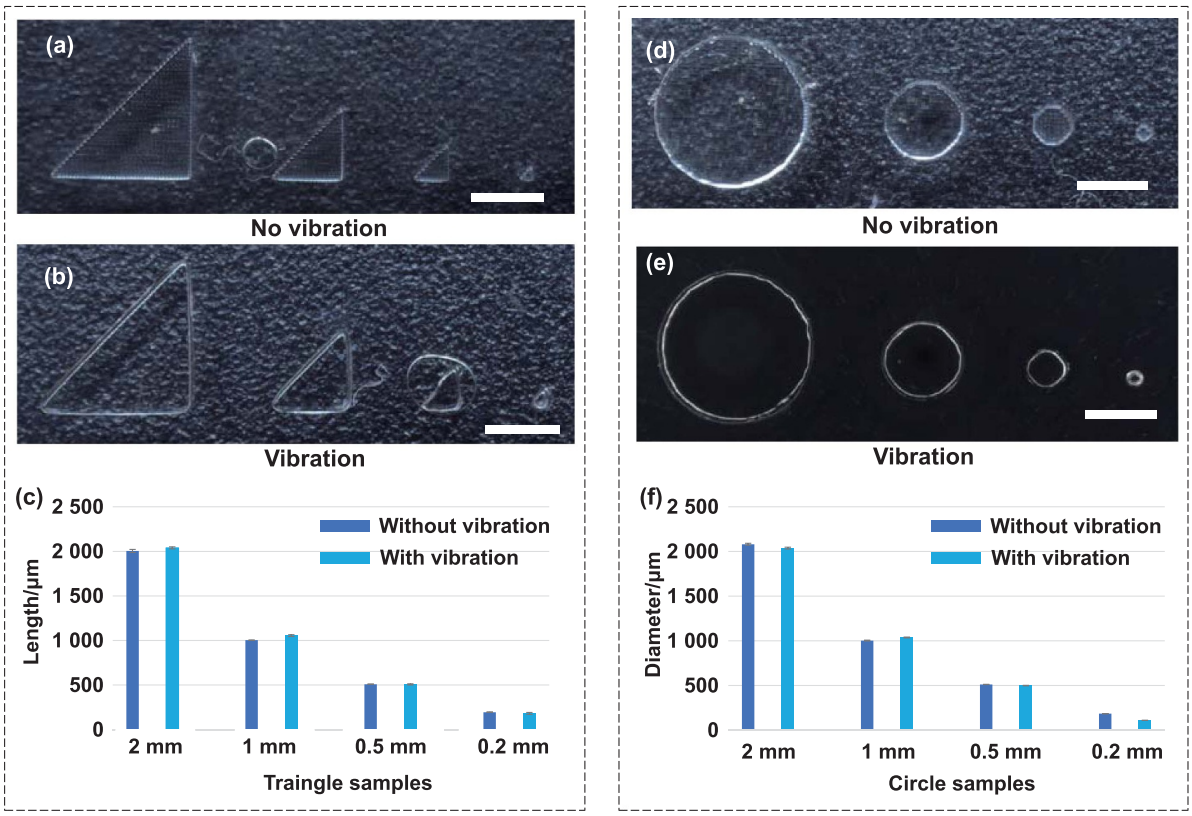

Figure 10. The dimensional accuracy of the test cases printed by vibration-assisted MIP-VPP, scale bar: 1 mm. (a) The triangle samples printed without vibration; (b) the triangle samples printed with a 3 × 4 steps vibration; (c) a comparison of the length of the bottom side between triangle samples printed with and without vibration; (d) the circle samples printed without vibration; (e) the circle samples printed with a 3 × 4 steps vibration; and (f) a comparison of the length of the bottom side between circle samples printed with and without vibration.

roughness of general geometries, as shown in figures S7 and S8.

We further study the effect of additional vibration on the dimensional accuracy for MIP-VPP. Here, we measure the dimensions of test cases printed by the vibration-assisted MIP-VPP process and compare them to the nominal dimensions. Cylinder and triangle test cases designed with characteristic dimensions of 2 mm, 1 mm, 0.5 mm, and 200 μm were printed and measured to validate the dimensional accuracy for various shape sizes from dimensions far bigger than a pixel size to a small one comparable to a pixel size. Figures 10(a) and (d) show the samples printed by the conventional MIP-VPP. Figures 10(b) and (e) show the samples printed by the vibration-assisted MIP-VPP. Figures 10(c) and (f) show the characteristic dimensions of the triangle and circle test cases. Both triangle and circle test cases show less than 50 μm error between the two fabrication processes. This indicates that the vibration-assisted MIP-VPP process does not significantly impact the overall dimensional accuracy. For larger parts with characteristic dimensions greater than 500 μm, it was observed that the printed parts using vibration-assisted MIP-VPP had a controlled size difference (between 10 μm and 50 μm) compared with those printed using the conventional MIP-VPP process. This discrepancy can be attributed to the amplitude of vibration in both X and Y directions, which leads to a dimensional change. In contrast, for parts with a length of diameter dimensions smaller than 200 μm, the parts printed using vibration-assisted VPP were found to be distorted because of XY vibration of the mask image. This phenomenon can be explained by the fact that at 200 μm scale, 50 μm shifting of the mask image becomes significant, thus changing the shape of the parts. The geometric distortion of the parts printed by vibration-assisted MIP-VPP is also studied in figure S10. These findings suggest that the vibration-assisted MIP-VPP

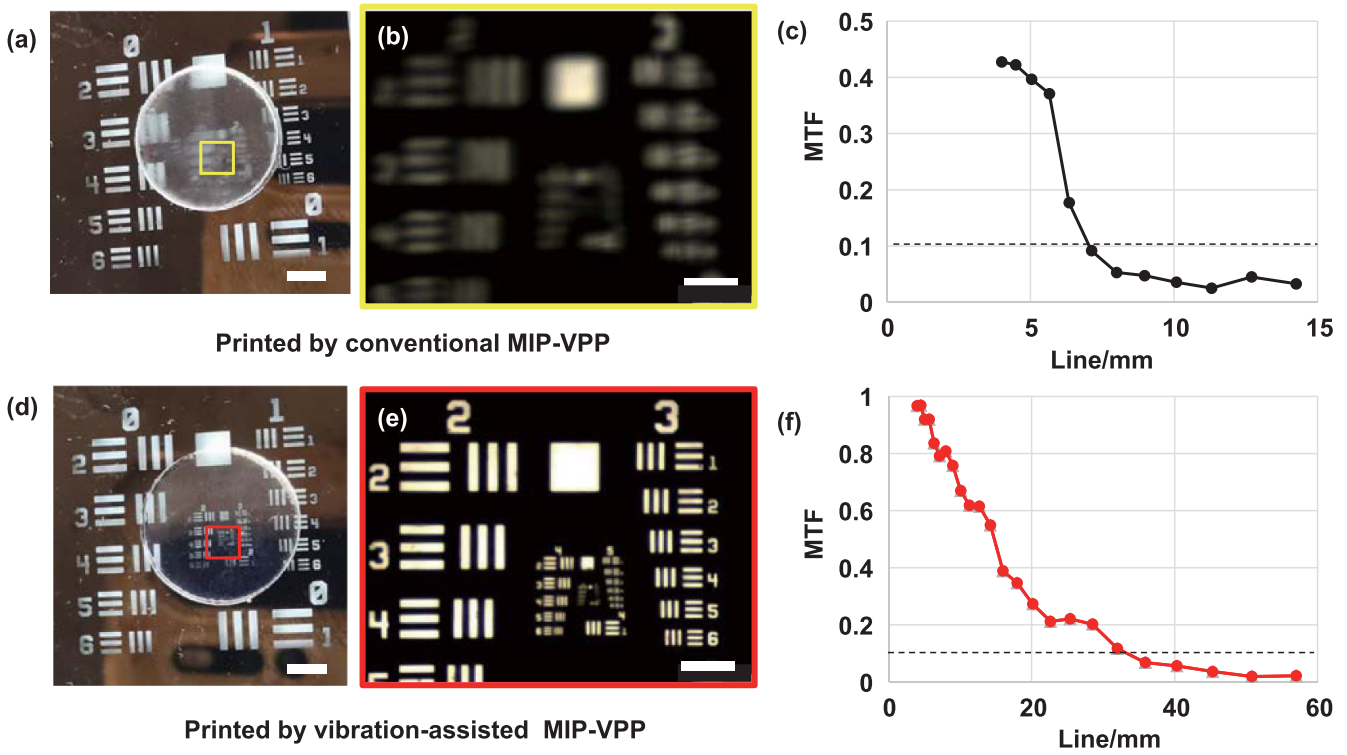

Figure 11. The resolving capability of a disc test case printed by the vibration-assisted MIP-VPP. (a) The disc test case printed by the conventional MIP-VPP; (b) the image of the USAF 1951 calibration target taken through the sample shown in (a); (c) the modulation transfer function of the sample shown in (a) over the grating density; (d) the disc test case printed by vibration-assisted MIP-VPP; (e) the image of the USAF 1951 calibration target taken through the sample shown in (d); and (f) the modulation transfer function of the sample shown in (d).

process offers comparable dimensional accuracy to the conventional VPP process when the fabrication dimensions are larger than 500 μm.

A smoother surface minimizes diffraction and scattering in 3D-printed parts. Hence, the vibration-assisted MIP-VPP process allows *in-situ* fabrication of products with high resolving capabilities, which are crucial for optical devices [33]. The MTF was used as a metric to evaluate the resolving capability of 3D-printed parts. The USAF 1951 calibration target was employed to measure the MTF of the resolution pattern through the 3D-printed parts. Figure 11 demonstrates the image-resolving capability of 3D-printed flat disc samples, which have a diameter of 9 mm and a thickness of 2 mm. Figures 11(a)–(c) show the image-resolving capability measured from the disc sample printed by conventional MIP-VPP without vibration. Figures 11(d)–(f) show the image-resolving capability measured from the disc sample printed by the vibration-assisted MIP-VPP (with a 3 $\times$ 4 steps vibration). Figures 11(b) and (e) show the zoom-in photos of the calibration target appearing through the printed discs. We can observe the difference between the samples printed without and with vibration, and the calibration target is significantly more apparent when vibration is employed in MIP-VPP printing. Figures 11(c) and (f) display the MTF of the printed discs. As the grating density increases, the MTF decreases for samples. However, the printed disc with vibration-assisted exhibits a slower MTF decrease than the printed disc with no vibration, indicating superior resolving capability. When the MTF falls below 10%, the contrast of the grating pattern is deemed unrecognizable. For the vibrated-assisted 3D-printed disc, the smallest distinguishable feature of the calibration target is 32 lines mm^{-1}, while the corresponding feature for the non-vibrated disc is only 7 lines mm^{-1}. This superior MTF performance across all grating patterns highlights the enhanced resolving capability of the vibration-assisted 3D-printed parts.

4. Discussion

The experimental results show that the surface roughness and boundary segment roughness of the parts printed by vibration-assisted MIP-VPP are significantly improved compared to the static binary and grayscale MIP-VPP methods. Increasing the number of vibration steps makes the surfaces' grid texture less prominent, resulting in a smoother surface. A 3 $\times$ 4 steps of vibration in the X and Y directions suffices to reduce light intensity variations to below 5% and reduce the surface roughness from 0.237 μm to 0.067 μm. For a typical exposure time of 4–6 s per layer, such a modest vibration (2–3 Hz) does not necessitate high-frequency operation, diminishing the hardware demands in the vibration-assisted MIP-VPP process. The combination of vibration-assisted and grayscale MIP-VPP offers the best boundary segment smoothness

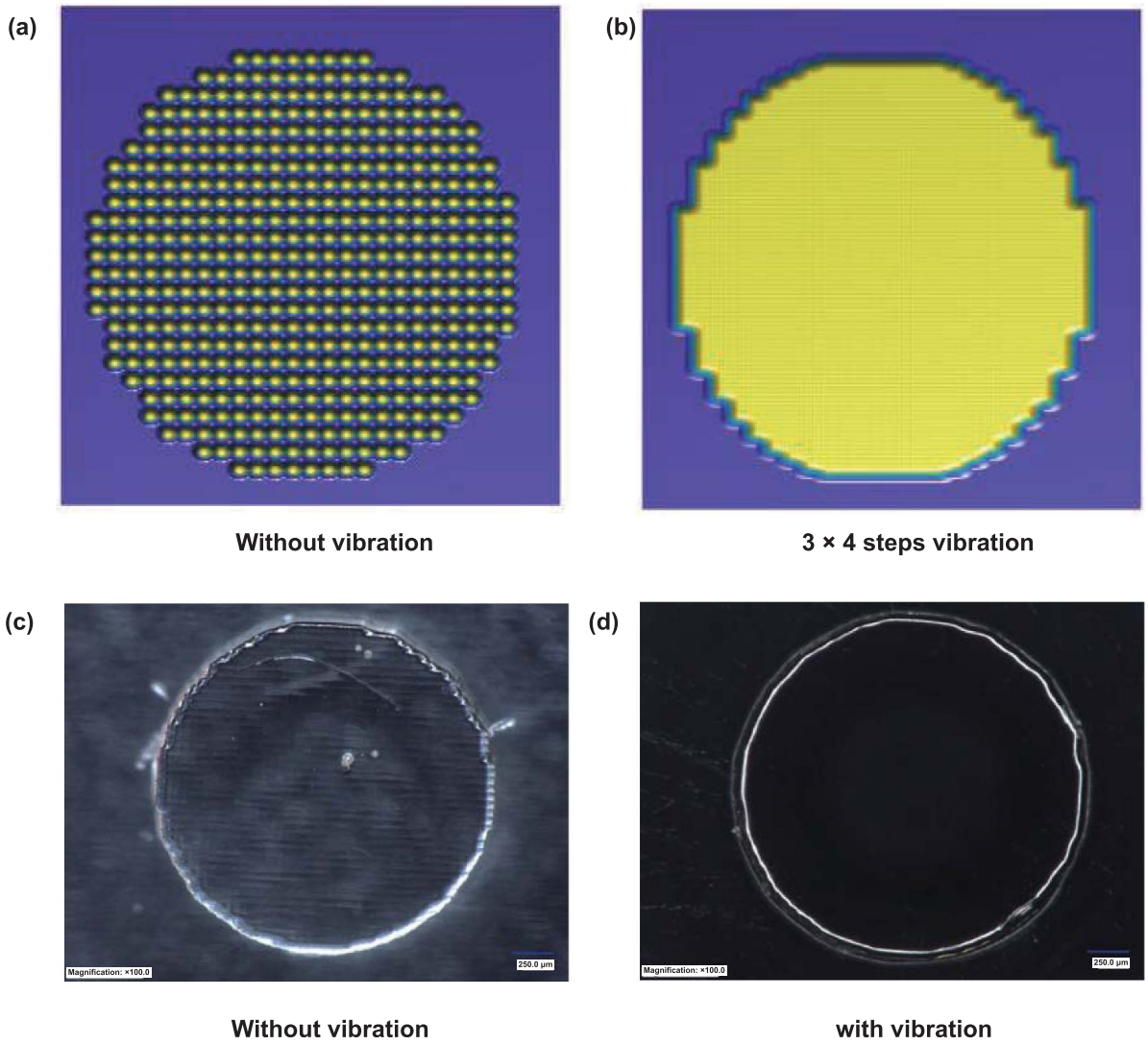

Figure 12. The effect of vibration-assisted MIP-VPP on curve features. (a) The simulated curing results of the circle test cases printed without vibration; (b) the simulated curing results of the circle test cases printed with vibration; (c) the 3D-printed circle test cases without vibration; and (d) the 3D-printed circle test cases with vibration.

(1.8 μm) compared to the one printed by binary mask images (8.0 μm), making it an ideal solution for applications requiring high-quality surface finish. Unlike other surface roughness-improving processes, such as defocusing MIP-VPP [19] and meniscus coating [24, 34], the vibration-assisted MIP-VPP improves the surface roughness with minimal dimensional inaccuracy. This unique advantage sets it apart from other techniques and further emphasizes its potential in various applications where surface quality and dimensional accuracy are paramount.

Although the vibration-assisted MIP-VPP process demonstrates promising results, it also presents certain limitations and challenges that need to be addressed. One of such limitations is the boundary roughness of a curve feature. As shown in figures 12(a) and (b), the vibration-assisted MIP-VP cannot improve the boundary roughness of the circle test case. The simulation of the curing results shows that the saw-teeth contour remains unchanged after the applied vibration with 3 $\times$ 4 steps or even more steps. These simulation results are verified by the physically 3D-printed test cases shown in figures 12(c) and (d). Further research and development efforts on vibration-assisted MIP-VPP, such as dynamically changing mask images during vibration [30], are needed to optimize curved features' dimensional and shape accuracy. Besides, the vibrations can introduce dimensional error and shape distortion when the feature size is smaller than 300 μm. This error prevents the vibration-assisted MIP-VPP from fabricating high-resolution features. Future work on addressing the limitations of printing small sizes with smooth features will be studied, such as investigating shape-dependent vibration patterns to improve dimensional accuracy for different part sizes. Additionally, we will explore potential applications in areas such as bioprinting, optics, and other emerging fields to expand the application ranges of this low-cost AM technique.

5. Conclusion

This work presents a method of applying a subpixel-level vibration to the mask images defined by an LCD screen to significantly improve the surface and boundary segment smoothness of products printed using MIP-VPP. This subpixel vibration technique equalizes the light intensity within the 'dark zone' of the mask images, mitigating the pixelated staircasing effect along the boundary line segments. By surpassing the limitations imposed by LCD's pixel size, this approach empowers commercial MIP-VPP equipment to produce components with submicron-level surface smoothness. The implications of this advancement are vast, holding substantial potential for a wide variety of applications in areas like customized optics, sensors, and microfluidic devices. The principle demonstrated in the study also paves the way for future innovations and improvements in MIP-VPP technology to achieve new heights of surface smoothness and accuracy.

Acknowledgments

The authors acknowledge the help of Dr Huachao Mao and Mr. Shutao Cai who worked at USC's CAM and built the piezo-driven linear stage used in the study. The authors also acknowledge Professor Hangbo Zhao at USC for his help with imaging and measurements.

CRediT authorship contribution statement

Han Xu: original draft-writing, data analysis, simulation, visualization, Renzhi Hu: original draft-writing, visualization, data curation, Shuai Chen: data curation, software, Junhong Zhu: data curable, hardware, Chi Zhou: draft-review and revision, and Yong Chen: conceptualization, methodology, supervision, original draft-review, and revision.

Conflict of interest

The authors declare that they have no known competing financial interests or personal relationships that could have appeared to influence the work reported in this paper.

ORCID iDs

Chi Zhou https://orcid.org/0000-0001-7230-3754
Yong Chen https://orcid.org/0000-0002-8377-5914

References

[1] Kruth J P, Leu M C and Nakagawa T 1998 Progress in additive manufacturing and rapid prototyping *CIRP Ann.* **47** 525–40
[2] Ashley S 1991 Rapid prototyping systems *Mech. Eng.* **113** 34–43
[3] Tumbleston J R *et al* 2015 Continuous liquid interface production of 3D objects *Science* **347** 1349–52
[4] Walker D A, Hedrick J L and Mirkin C A 2019 Rapid, large-volume, thermally controlled 3D printing using a mobile liquid interface *Science* **366** 360–4
[5] Xu Y, Zhu Y Z, Sun Y F, Jin J and Chen Y 2021 A vibration-assisted separation method for constrained-surface-based stereolithography *J. Manuf. Sci. Eng.* **143** 051008
[6] Xu Y, Mao H C, Liu C Y, Du Z Y, Yan W J, Yang Z Y, Partanen J and Chen Y 2023 Hopping light vat photopolymerization for multiscale fabrication *Small* **19** 2205784
[7] Zhou C, Chen Y, Yang Z G and Khoshnevis B 2013 Digital material fabrication using mask-image-projection-based stereolithography *Rapid Prototyp. J.* **19** 153–65
[8] Xu H, Chen S, Hu R Z, Hu M Q, Xu Y, Yoon Y and Chen Y 2023 Continuous vat photopolymerization for optical lens fabrication *Small* **19** 2300517
[9] Xu Y, Qi F J, Mao H C, Li S W, Zhu Y Z, Gong J W, Wang L, Malmstadt N and Chen Y 2022 In-situ transfer vat photopolymerization for transparent microfluidic device fabrication *Nat. Commun.* **13** 918
[10] Zhao C X, Jariwala A S and Rosen D W 2016 Real time monitoring of exposure controlled projection lithography with time-varying scanning points *Proc. 26th Annual Int. Solid Freeform Fabrication Symp.—An Additive Manufacturing Conf.* (University of Texas at Austin)
[11] Zhao X Y, Wang J M, Zhao C X, Jariwala A and Rosen D W 2016 Experimental implementation and investigation of real-time metrology for exposure controlled projection lithography *Proc. 26th Annual Int. Solid Freeform Fabrication Symp.—An Additive Manufacturing Conf.* (University of Texas at Austin)
[12] Milton L A, Viglione M S, Ong L J Y, Nordin G P and Toh Y C 2023 Vat photopolymerization 3D printed microfluidic devices for organ-on-a-chip applications *Lab Chip* **23** 3537–60
[13] Shao G B, Hai R H and Sun C 2020 3D printing customized optical lens in minutes *Adv. Opt. Mater.* **8** 1901646
[14] Chen X F, Liu W Z, Dong B Q, Lee J, Ware H O T, Zhang H F and Sun C 2018 High-speed 3D printing of millimeter-size customized aspheric imaging lenses with sub 7 nm surface roughness *Adv. Mater.* **30** 1705683
[15] Yuan C, Kowsari K, Panjwani S, Chen Z C, Wang D, Zhang B, Ng C J X, Alvarado P V Y and Ge Q 2019 Ultrafast three-dimensional printing of optically smooth microlens arrays by oscillation-assisted digital light processing *ACS Appl. Mater. Interfaces* **11** 40662–8
[16] Lai H W *et al* 2020 Consensus statement on robotic mastectomy—expert panel from international endoscopic and robotic breast surgery symposium (IERBS) 2019 *Ann. Surg.* **271** 1005–12
[17] Odent J, Baleine N, Biard V, Dobashi Y, Vancaeyzeele C, Nguyen G T M, Madden J D W, Plesse C and Raquez J M 2023 3D-printed stacked ionic assemblies for iontronic touch sensors *Adv. Funct. Mater.* **33** 2210485
[18] Paral S K, Lin D Z, Cheng Y L, Lin S C and Jeng J Y 2023 A review of critical issues in high-speed vat photopolymerization *Polymers* **15** 2716
[19] Shan Y J, Krishnakumar A, Qin Z H and Mao H C 2022 Reducing lateral stair-stepping defects in liquid crystal display-based vat photopolymerization by defocusing the image pattern *Addit. Manuf.* **52** 102653
[20] Vaezi M and Chua C K 2011 Effects of layer thickness and binder saturation level parameters on 3D printing process *Int. J. Adv. Manuf. Technol.* **53** 275–84

[21] Gao W, Zhang Y B, Ramanujan D, Ramani K, Chen Y, Williams C B, Wang C C L, Shin Y C, Zhang S and Zavattieri P D 2015 The status, challenges, and future of additive manufacturing in engineering *Comput.-Aided Des.* **69** 65–89
[22] Chen H W, Lee J H, Lin B Y, Chen S and Wu S T 2018 Liquid crystal display and organic light-emitting diode display: present status and future perspectives *Light Sci. Appl.* **7** 17168
[23] Mao H C, Kwok T H, Chen Y and Wang C C L 2019 Adaptive slicing based on efficient profile analysis *Comput.-Aided Des.* **107** 89–101
[24] Pan Y Y and Chen Y 2016 Meniscus process optimization for smooth surface fabrication in Stereolithography *Addit. Manuf.* **12** 321–33
[25] Namgung H, Kaba A M, Oh H, Jeon H, Yoon J, Lee H and Kim D 2022 Quantitative determination of 3D-printing and surface-treatment conditions for direct-printed microfluidic devices *BioChip J.* **16** 82–98
[26] Heinrich A, Rank M, Maillard P, Suckow A, Bauckhage Y, Rößler P, Lang J, Shariff F and Pekrul S 2016 Additive manufacturing of optical components *Adv. Opt. Technol.* **5** 293–301
[27] Zhou C, Chen Y and Waltz R A 2009 Optimized mask image projection for solid freeform fabrication *J. Manuf. Sci. Eng.* **131** 061004
[28] Zhou C and Chen Y 2012 Additive manufacturing based on optimized mask video projection for improved accuracy and resolution *J. Manuf. Process.* **14** 107–18
[29] Gong H, Beauchamp M, Perry S, Woolley A T and Nordin G P 2015 Optical approach to resin formulation for 3D printed microfluidics *RSC Adv.* **5** 106621–32
[30] Zhou C, Xu H and Chen Y 2021 Spatiotemporal projection-based additive manufacturing: a data-driven image planning method for subpixel shifting in a split second *Adv. Intell. Syst.* **3** 2100079
[31] Gao X Y, Yang J K, Wu J G, Xin X D, Li Z M, Yuan X T, Shen X Y and Dong S X 2020 Piezoelectric actuators and motors: materials, designs, and applications *Adv. Mater. Technol.* **5** 1900716
[32] Liu Y F, Shan J J and Gabbert U 2015 Feedback/feedforward control of hysteresis-compensated piezoelectric actuators for high-speed scanning applications *Smart Mater. Struct.* **24** 015012
[33] Alam F, Elsherif M, AlQattan B, Salih A, Lee S M, Yetisen A K, Park S and Butt H 2021 3D printed contact lenses *ACS Biomater. Sci. Eng.* **7** 794–803
[34] Pan Y Y, He H Y, Xu J and Feinerman A 2017 Study of separation force in constrained surface projection stereolithography *Rapid Prototyp. J.* **23** 353–61